Inorg. Chem. **2008**, *47*, 7577−7587

Inorganic Chemistry

Article

Temperature-Dependent Interactions and Disorder in the Spin-Transition Compound $[Fe^{II}(L)_2][ClO_4]_2 \cdot C_7H_8$ Through Structural, Calorimetric, Magnetic, Photomagnetic, and Diffuse Reflectance Investigations

Vibha Mishra,[†,‡] Rabindranath Mukherjee,[‡] Jorge Linares,[†] Chérif Balde,[§] Cédric Desplanches,[§] Jean-François Létard,[§] Eric Collet,[||] Loic Toupet,[||] Miguel Castro,[⊥] and François Varret*[,†]

GEMAC, CNRS—Université de Versailles, 78035 Versailles cedex, France, Department of Chemistry, Indian Institute of Technology Kanpur, Kanpur 208 016, India, ICMCB, CNRS, Université Bordeaux 1, 87, avenue du Dr. A. Schweitzer, 33608 Pessac cedex, France, Université de Rennes 1, Institut de Physique de Rennes, UMR UR1-CNRS 6251, Campus Beaulieu, F-35042 Rennes, France, and Instituto de Ciencia de Materiales de Aragon (CSIC-Universidad de Zaragoza)—Pendro Cerbuna 12, 5009 Zaragoza, Spain

Received February 16, 2008

The title compound $[Fe^{II}(L)_2][ClO_4]_2 \cdot C_7H_8$ (L = 2-[3-(2′-pyridyl)pyrazol-1-ylmethyl]pyridine) has been isolated while attempting to grow single crystals of the spin-transition (continuous-type) compound $[Fe^{II}(L)_2][ClO_4]_2$, published earlier (*Dalton Trans.* **2003**, 3392−3397). Magnetic susceptibility measurements, as well as Mössbauer and calorimetric investigations on polycrystalline samples of $[Fe(L)_2][ClO_4]_2 \cdot C_7H_8$ revealed the occurrence of an abrupt HS ($^5T_2$) ↔ LS ($^1A_1$) transition with steep and narrow (2 K) hysteresis at ∼232 K. The photomagnetic properties exhibit features typical for a broad distribution of activation energies, with relaxation curves in the shape of stretched exponentials. We performed a crystal structure determination of the compound at 120, 240, and 270 K. A noteworthy temperature-dependent behavior of the structural parameters was observed, in terms of disorder of both the anions and solvent molecules, leading to a strong thermal dependence of the strength and dimensionality of the interaction network. Additional data were obtained by diffuse reflectance measurements. We model and discuss the antagonistic effects of interactions and disorder by using a two-level cooperative mean-field approach which includes a distribution of barrier energies at the microscopic scale.

Introduction

The coordination chemistry of pyrazole-derived chelating ligands,[1] in addition to well-known tris(pyrazolyl)borates,[2] has been vigorously developed. A few years back, we reported that the nonplanar tridentate ligand 2-[3-(2′-pyridyl)pyrazol-1-ylmethyl]pyridine (L) forms bis-ligand complexes with transition metal ions, including a demonstration of temperature-induced spin-transition for the iron(II) compound $[Fe(L)_2][ClO_4]_2$.[3] In the bis-ligand complex, the metal ion is surrounded by two pyrazole and four pyridyl groups, with electronic communication between the pyridylpyrazole unit and 2-pyridylmethyl arm prevented, due to the presence of a methylene spacer. The present investigation stems from our effort to grow single crystals of $[Fe(L)_2][ClO_4]_2$ from MeCN/toluene. In contrast to its nonsolvated variety, the isolated microcrystalline product with the composition $[Fe^{II}(L)_2][ClO_4]_2 \cdot C_7H_8$ was found to exhibit a steep spin-transition with a narrow hysteresis loop. This phenomenon illustrates the demonstrated role of solvent molecules present as a solvent of crystallization,[4,5] which may contribute to

---

* To whom correspondence should be addressed. E-mail: fvarret@physique.uvsq.fr.

[†] CNRS—Université de Versailles.

[‡] Indian Institute of Technology Kanpur.

[§] Université Bordeaux 1.

[||] Université de Rennes 1.

[⊥] Instituto de Ciencia de Materiales de Aragon.

(1) Mukherjee, R. *Coord. Chem. Rev.* **2000**, *203*, 151, and references therein.

(2) Trofimenko, S. *Scorpionates - The Coordination Chemistry of Polypyrazolylborate. Ligands*; Imperial College Press: London, 1999.

(3) (a) Singh, S.; Mishra, V.; Mukherjee, J.; Seethalekshmi, N.; Mukherjee, R. *Dalton Trans.* **2003**, 3392. (b) Halcrow, M. A. *Polyhedron* **2007**, *26*, 3523. (c) Real, J. A.; Gaspar, A. B.; Munoz, M. C. *Dalton Trans.* **2005**, 2062.

(4) Toftlund, H. *Coord. Chem. Rev.* **1989**, *94*, 67.

10.1021/ic8002977 CCC: $40.75

the cooperative character of the spin-transition due to noncovalent interactions (hydrogen-bonding or $\pi-\pi$ stacking) or van der Waals interactions.[5,6]

In the course of the present investigation, we observed the coexistence of two conflicting phenomena, with effects of unprecedented magnitude. These are (i) a steep spin-transition with a narrow hysteresis loop, which implies the presence of cooperative interactions,[7] and (ii) a stretched exponential nature of the relaxation curves of the photoexcited state, which is usually ascribed to some structural disorder, resulting in a distribution of energy barriers among other physical parameters.[8] Such relaxation curves were recently analyzed[9] with $[Fe(L')_2][ClO_4]_2\cdot H_2O$ [L′ = 2,6-bis(pyrazol-1-ylmethyl)pyridine]. The quantitative account of antagonistic factors has remained a rare phenomenon[8b,10] and has been mainly used for the reconciliation of interaction parameters separately derived from the thermal hysteresis loop and the relaxation curves. The origin of disorder was an order/disorder phase transition,[8b] and the local disorder was assigned to the nonstoichiometric character of the compound (a photomagnetic Prussian blue analogue),[10] responsible for a relatively minor modulation of the energy barrier at the microscopic scale, while the long-range elastic interaction could be treated in the mean-field approach. Such a distinction between macroscopic and microscopic scale for the disorder effect is the vital difference between the cooperative models used in the quoted works.[8b,10] We stress that the mean-field approach which treats the interaction terms may include local modulations of the barrier energy, which is a single-site property. To the best of our knowledge, no cooperative static model has been so far extended for the inclusion of disorder on the microscopic scale. It was the virtue of the macroscopic master equation, based of cooperative relaxation terms, to allow an easy extension to the case of microscopic distributions of single-molecule properties.[11]

Herein, we provide a detailed account of the results of our investigation on the title compound $[Fe^{II}(L)_2][ClO_4]_2\cdot C_7H_8$. This report shows how optical and structural studies could be combined to elucidate the origin of the complex behavior of the title compound. For the reader's convenience, we list here the acronyms used in the course of the report, with suggested basic references: HS (high-spin) and LS (low-spin) states,[12] LIESST (light-induced excited spin-state trapping),[13] and LITH (light-induced thermal hysteresis).[14]

Experimental Section

Materials and Reagents. All chemicals were obtained from commercial sources and used as received. Solvents were purified/dried following standard procedures.[3] The ligand (L) 2-[3-(2′-pyridyl)pyrazol-1-ylmethyl]pyridine was prepared as before,[3] and 3-(2-pyridyl)pyrazole was synthesized following a reported procedure.[4]

Synthesis of $[Fe^{II}(L)_2][ClO_4]_2\cdot C_7H_8$. $[Fe(L)_2][ClO_4]_2$ (0.050 g, 0.07 mmol) was dissolved in MeCN (3 mL), followed by the slow addition of toluene (10 mL). This mixture was then allowed to stand overnight in a fridge, which led to the precipitation of a yellow microcrystalline solid. It was filtered and dried in vacuo (yield: 0.045 g, *ca.* 80%).

Physical Measurements. Elemental analyses were obtained at the Microanalytical Laboratory at the Department of Chemistry, Indian Institute of Technology Kanpur. Found: C, 51.34; H, 3.90; N, 13.70. Calcd for $C_{35}H_{32}N_8Cl_2FeO_8$ (818.84): C, 51.30; H, 3.90; N, 13.68%. Infrared spectra were recorded on a Bruker Vector 22 spectrophotometer using KBr discs.

X-Ray Crystallography. X-ray data collection on the compound $[Fe^{II}(L)_2][ClO_4]_2\cdot C_7H_8$ was performed at 270, 240 (high-spin state), and 120 K (low-spin state) on a four-circle diffractometer with a two-dimensional CCD detector. The single crystals were mounted on an Oxford Cryosystems nitrogen-flow cryostat for measurements down to 78 K, with a temperature stability of 0.1 K. An Oxford Diffraction Helijet helium-flow cryostat (which allows for reaching 20 K with a temperature stability of 0.5 K) was used to investigate the LIESST effect induced by laser irradiation at 532 nm. The unit-cell parameters and data reduction were obtained with *CrysAlis* software from Oxford Diffraction.[15] Intermolecular contacts of the $C-H\cdots\pi$ and $C-H\cdots O$ types were examined with the DIAMOND package.[16] The C−H distances were normalized along the same vectors to the neutron-derived value of 1.083 Å.[17] The structure was solved in the space group $P2_1/n$ with *SIR97* and refined with *SHELXL9*.[18] Absorption correction was not necessary, with absorption coefficient $\mu = 0.615$ mm^{-1} and a crystal thickness of 0.2 mm. The CCDC reference numbers are 675817−675819. Structure refinement data are reported in Table 1.

Magnetic and Mössbauer Measurements. Magnetic measurements were done using a SQUID magnetometer (Quantum design MPMS5) operating at a magnetic field of 1 kOe. Susceptibilities

---

(5) Gütlich, P. In *Topics in Current Chemistry: Spin Crossover in Transition Metal Compounds*; Gütlich, P., Goodwin, H. A., Eds.; Springer: New York, 2004; Vol. *233*, pp 1−47.

(6) (a) Leita, B. A.; Neville, S. M.; Halder, G. J.; Moubaraki, B.; Kepert, C. J.; Létard, J.-F.; Murray, K. S. *Inorg. Chem.* **2007**, *46*, 8784. (b) Yamada, Y.; Fukumoto, E.; Ooidemizu, M.; Bréfuel, N.; Matsumoto, N.; Iijima, S.; Kojima, M.; Re, N.; Dahan, F.; Tuchagues, J.-P. *Inorg. Chem.* **2005**, *44*, 6967.

(7) (a) Spiering, H. In *Topics in Current Chemistry: Spin Crossover in Transition Metal Compounds*; Gütlich, P., Goodwin, H. A., Eds.; Springer: New York, 2004, Vol. *234*, p 129. (b) Murray, K. S.; Kepert, C. J. In *Topics in Current Chemistry: Spin Crossover in Transition Metal Compounds*; Gütlich, P., Goodwin, H. A., Eds.; Springer: New York, 2004, Vol. *233*, p 195.

(8) (a) Hauser, A.; Adler, J.; Gütlich, P. *Chem. Phys. Lett.* **1988**, *152*, 468. (b) Hauser, A.; Jeftic, J.; Romstedt, H.; Hinek, R.; Spiering, H. *Coord. Chem. Rev.* **1999**, *192*, 471.

(9) Enachescu, C.; Linarès, J.; Varret, F.; Boukheddaden, K.; Codjovi, E.; Gawali-Salunke, S.; Mukherjee, R. *Inorg. Chem.* **2004**, *43*, 4880.

(10) (a) Gawali-Salunke, S.; Varret, F.; Maurin, I.; Malarova, M.; Enachescu, C.; Boukheddaden, K.; Codjovi, E.; Tokoro, H.; Ohkoshi, S.; Hashimoto, K. *J. Phys. Chem. B* **2005**, *109*, 8251. (b) Castro, M.; Rodríguez-Velamazán, J. M.; Boukheddaden, K.; Varret, F.; Tokoro, H.; Ohkoshi, S. *Eur. Phys. Lett.* **2007**, *79*, 27007.

(11) Varret, F.; Boukheddaden, K.; Codjovi, E.; Maurin, I.; Tokoro, H.; Ohkoshi, S.; Hashimoto, K. *Polyhedron* **2005**, *24*, 2857.

(12) *Topics in Current Chemistry: Spin Crossover in Transition Metal Compounds*; Gütlich, P., Goodwin, H. A., Eds.; Springer: New York, 2004; three volumes.

(13) (a) Decurtins, S.; Gütlich, P.; Kohler, C. P.; Spiering, H.; Hauser, A. *Chem. Phys. Lett.* **1984**, *139*, 1. (b) Hauser, A. *Chem. Phys. Lett.* **1984**, *124*, 543.

(14) (a) Létard, J.-F.; Guionneau, P.; Rabardel, L.; Howard, J. A. K.; Goeta, A. E.; Chasseau, D.; Kahn, O. *Inorg. Chem.* **1998**, *37*, 4432. (b) Desaix, A.; Roubeau, O.; Jeftic, J.; Haasnoot, J. G.; Boukheddaden, K.; Codjovi, E.; Linarès, J.; Nogues, M.; Varret, F. *Eur. Phys. J. B* **1998**, *6*, 183.

(15) *CrysAlis*; Oxford: Oxfordshire, U.K.

(16) *DIAMOND*, ver 2.1c; Crystal Impact GbR: Bonn, Germany, 1999.

(17) Steiner, T. *Angew. Chem., Int. Ed.* **2002**, *41*, 48.

(18) Sheldrick, M. *SHELX97*; University of Göttingen, Göttingen, Germany, 1997.

Table 1. Crystallographic Data at 270, 240, and 120 K for $[Fe(L)_2][ClO_4]_2\cdot C_7H_8$

M_r/g	819.4	819.4	819.4
temp/K	270(2)	240(2)	120(2)
radiation used (λ/Å)	Mo Kα (0.71069)	Mo Kα (0.71069)	Mo Kα (0.71069)
cryst syst	monoclinic	monoclinic	monoclinic
space group	$P2_1/n$ (no. 14)	$P2_1/n$ (no. 14)	$P2_1/n$ (no. 14)
a/Å	14.157(2)	14.020(1)	13.737(3)
b/Å	19.279(3)	19.279(1)	18.687(4)
c/Å	13.986(3)	14.169(1)	13.741(3)
α/deg	90.000	90.000	90.000
β/deg	104.39(1)	105.042(4)	97.92(2)
γ/deg	90.000	90.000	90.000
V/Å	3697.50(11)	3698.5(4)	3493.9(1)
Z	4	4	4
D_c/g cm^{-3}	1.472	1.472	1.56
μ/mm^{-1}	0.615	0.615	0.651
cryst size/mm	0.25 × 0.15 × 0.15	0.25 × 0.15 × 0.15	0.25 × 0.15 × 0.15
unique reflns, R_{int}	10280, 0.1331	31976, 0.1331	11013, 0.1175
obsd reflns ($I > 2\sigma(I)$)	1812	3713	3800
refined params	515	552	487
R^a $(R_w)^a$	0.0757 (0.2897)	0.0616 (0.1512)	0.0597 (0.1422)
R^a $(R_w)^a$ (all data)	0.1712 (0.2060)	0.1749 (0.2060)	0.1307 (0.1472)
goodness-of-fit on F^2	0.673	0.748	0.924

^{a} $R(F) = \sum(||F_o| - |F_c||)/\sum|F_o|$. $R_w(F^2) = \{\sum[w(|F_o|^2 - |F_c|^2)^2]/\sum[w(|F_o|^2)^2]\}^{1/2}$.

were corrected for diamagnetic contributions, by using literature values.[19] Effective magnetic moments were calculated from $\mu_{eff} = 2.828\,[\chi_M T]^{1/2}$, where χ_M is the corrected molar susceptibility.

Mössbauer spectra were recorded on a constant-acceleration spectrometer, with a 50 mCi source of ^{57}Co in a rhodium matrix. The polycrystalline absorber contained ~20 mg of material/cm^2. The typical experimental line width, in the useful velocity range, was ~0.215 mm/sec. The spectra, once folded, were fitted without correction of the thickness effect. Least-square-fitted parameters are given with their standard deviations of statistical origin (in brackets), and isomer shift values refer to natural iron at room temperature.

Calorimetric Experiments. Calorimetric data were obtained with a differential scanning calorimeter (DSC) Q1000 from TA Instruments in the 100−330 K temperature range and at a scan rate of 1 K/min. The measurements were carried out using 3.88 mg of powdered sample sealed in aluminum pans with a mechanical crimp. Standard samples of indium, using its melting transition (429.76 K, 3.296 kJ/mol), and of Mn_3GaC, using its ferro- to antiferromagnetic transition (171.83 K, 713 J/mol), were used for the temperature and enthalpy calibrations. An overall accuracy of ±0.5 K in temperature and ±5% in the enthalpy contents is estimated. The uncertainty increases for the determination of the anomalous enthalpy and entropy, due to the difficulty involved with tracing the baselines (especially for the cooling mode).

Photomagnetic Experiments. Photomagnetic experiments were performed using a mixed gas Krypton/Argon Spectra Physics Beamlock 2060 ($\lambda = 514.5$ nm) coupled *via* an optical fiber to the cavity of a MPMS-55 Quantum Design SQUID magnetometer. The optical power at the sample surface was adjusted to 5 mW cm^{-2}. Photomagnetic samples consisted of a thin layer of the compound spread over 0.1 cm^2 whose weight (0.1 mg) was obtained by comparing the thermal spin-crossover curve to that of an accurately weighted bulk sample.[20] The thermal return temperature T(LIESST) was determined by following the standard method reported by Létard and co-workers.[21]

Diffuse Reflectance. Diffuse absorption spectra and the reflectivity signal were recorded using a custom-built setup equipped with a SM240 spectrometer (Opton Laser International). This equipment allows the diffuse reflectance spectra, within a range of 500−900 nm at a given temperature, and the temperature dependence (5−290 K) of the reflectivity signal at a selected wavelength (±2.5 nm) to be recorded. The diffuse reflectance spectrum was calibrated with respect to activated charcoal (Merck) as a black standard and barium sulfate ($BaSO_4$, Din 5033, Merck) as a white standard. This analysis was performed directly on a thin layer of polycrystalline powders; no dispersion in a matrix was required.

Simulation. We simulated the variations of the high-spin fraction (n_{HS}) in a mean-field two-level approach, using a macroscopic master equation (actually, a rate equation in chemical terms) suitable for reproducing both static and kinetic properties,[11] defined as follows:

$$dn/dt = [1 - n(t)] \times [k_{opt} + k_{LH}(T, n)] - n(t) \times k_{HL}(T, n) \tag{1}$$

where $n(t)$ is the HS fraction, $k_{opt} = I_{LH}\sigma_{LS}\eta_{LS}$ accounts for the light intensity, as well as for the absorption cross-section and the quantum yield, and $k_{HL}(T,n)$ is the rate constant of the HS → LS relaxation. In a first approach, the quantum yield is assumed to be constant, and the self-accelerated relaxation rate constants following the internal pressure concept[22] can be expressed as

$$k_{HL}(T, n) = k_{HL}(T)\,\exp[-\alpha(n - 1/2)] \tag{2}$$

$$k_{LH}(T, n) = k_{LH}(T)\,\exp[+\alpha(n - 1/2)] \tag{3}$$

In the thermally activated regime, the "Hauser" self-acceleration factor[23] is proportional to the interaction parameter (zJ in an Ising-

---

(19) O'Connor, C. J. *Prog. Inorg. Chem.* **1982**, *29*, 203.

(20) Enachescu, C.; Varret, F.; Codjovi, E.; Linarès, J.; Floquet, S.; Manikandan, P.; Manoharan, P. T. *J. Phys. Chem. B* **2006**, *110*, 5883.

(21) (a) Létard, J.-F.; Guionneau, P.; Nguyen, O.; Costa, J. S.; Marcén, S.; Chastanet, G.; Marchivie, M.; Capes, L. *Chem.—Eur. J.* **2005**, *11*, 4582. (b) Létard, J.-F. *Mater. Chem.* **2006**, *16*, 2550. (c) Money, V. A.; Carbonera, C.; Elhaïk, J.; Halcrow, M. A.; Howard, J. A. K.; Létard, J.-F. *Chem.—Eur. J.* **2007**, *13*, 5503.

(22) Hauser, A.; Gütlich, P.; Spiering, H. *Inorg. Chem.* **1986**, *25*, 4245.

(23) Hauser, A. *Coord. Chem. Rev.* **1992**, *192*, 65.

like model) and inversely proportional to the temperature: $\alpha = 2zJ/k_BT$. The temperature-dependent factors are expressed as follows:

$$k_{HL}(T) = k_\infty \exp(-E_{HL}/k_BT) \tag{4}$$

$$k_{LH}(T) = gk_\infty \exp[-(E_{HL}+\Delta_{el})/k_BT] \tag{5}$$

where E_{HL} and Δ_{el} respectively are the energy barrier and energy gap between the excited HS state and the LS ground state, and $g = g_{HS}/g_{LS}$ is the effective degeneracy ratio. Inserting expressions 4 and 5 into the detailed balance equation (that is, eq 1 with $dn/dt = 0$) immediately yields the usual canonical expression for the spin equilibrium:

$$n/(1-n) = k_{LH}(T)/k_{HL}(T) = g \exp(-\Delta_{el}/k_BT) \exp[2\alpha(n-1/2)] \tag{6}$$

The microscopic quantities Δ_{el} and g involved in eq 6 are straightforwardly related to calorimetric data: molar entropy change upon complete spin conversion $\Delta S = R \ln g$ and molar enthalpy change $\Delta H = N\Delta_{el}$, with N being the Avogradro number. The static parameters g, Δ_{el}, and zJ govern the "static" conversion curve, that is, $n_{HS}(T)$ recorded at quasi-equilibrium (when the temperature scan rate is *slow* with respect to the relaxation rate constants). The kinetic parameters k_∞, E_{HL}, and αT, respectively, govern the time scale, the thermal dependence, and the shape of the relaxation curves and the kinetic effects which appear when the temperature scan rate is not slow with respect to the relaxation rate constants. The derivation of the specific heat from the master equation has been described in previous work[10b] for analyzing the thermal return from a thermally quenched state in a similar switchable system.

In the framework of recent works,[10] we introduced two spacio-temporal variants of the cooperative model: (i) macroscopic variants accounting for a Gaussian distribution of parameters over independent domains (Δ_{el} for the thermal transition and E_{HL} for the relaxation curves) and (ii) microscopic variants where the same Gaussian distributions are associated with crystallographic sites, allowing a *uniform* mean-field treatment of the interaction effects by *averaging* the self-acceleration factors at each computation step. The kinetic effects are straightforwardly modeled by numerical treatment of the master equation. The "static" thermal transition can also be modeled at the quasi-static limit by a convenient choice of the time scale. In other words, the resolution of the set of coupled nonlinear equations associated with the mutual interaction of local thermal equilibriums can be bypassed. Both macroscopic and microscopic distributions may, of course, coexist. At last, it must be mentioned that the difference between macroscopic and microscopic variants vanishes in the noncooperative case ($J = 0$).

The micro- and macroscopic models are not only alternative variants. They also account for disorder effects at different scales and may be combined. For this combination, a set of independent master equations has to considered, involving distributions of the central values of the microscopic distributions. The microscopic distributions account for short-range local effects such as atomic disorders on nonstochiometry effects. The macroscopic distributions account for eventual like-spin domain structures, for structural domains associated with extended defects, and for nonuniform properties of the polycrystalline state. The simulations showed that the hysteresis loop of the thermal (or light-induced) transition is differently impacted by the macro- and microscopic distributions. The microscopic distributions reduce the size of the loop—which remains square-shaped as long as the interaction parameter remains sufficiently large—while the macroscopic distributions are responsible for the bent character of the loop. To the contrary, the relaxation curves, due to their smooth character, do not allow a disentangling of the two kinds of distributions. For simplicity, we have considered separately the macro- and microscopic effects on the thermal transition: their combination would be time-consuming, for an obvious result. We have neglected the narrow macroscopic distribution determined at the thermal transition, when dealing with the relaxation and T(LIESST) curves.

Table 2. Selected Bond Lengths (Å) and Angles (deg) of $[Fe(L)_2][ClO_4]_2 \cdot C_7H_8$ at 270, 240, and 120 K

	270 K	240 K	120 K
Fe1−N(1)	2.198(6)	2.158(4)	1.985(3)
Fe1−N(2)	2.050(6)	2.057(3)	1.882(3)
Fe1−N(4)	2.213(6)	2.173(3)	2.027(3)
Fe1−N(21)	2.167(6)	2.185(4)	1.987(3)
Fe1−N(22)	2.026(6)	2.044(3)	1.872(3)
Fe1−N(24)	2.236(6)	2.235(4)	2.037(3)
N(1)−Fe1−N(2)	74.6(3)	74.12(14)	79.32(14)
N(1)− Fe1−N(4)	159.5(3)	160.19(14)	169.63(14)
N(1)−Fe1−N(21)	97.8(2)	97.64(13)	93.30(13)
N(1)−Fe1−N(22)	97.0(2)	97.64(14)	94.45(14)
N(1)−Fe1−N(24)	95.5(2)	95.48(13)	93.66(13)
N(2)−Fe1−N(4)	85.2(3)	86.27(14)	90.93(14)
N(2)−Fe1−N(21)	103.1(2)	101.62(14)	96.30(13)
N(2)−Fe1−N(22)	171.2(3)	170.98(15)	172.24(15)
N(2)−Fe1−N(24)	99.8(2)	100.35(14)	94.84(14)
N(4)−Fe1−N(21)	89.8(2)	88.91(13)	91.29(13)
N(4)−Fe1−N(22)	103.3(2)	102.11(14)	95.54(14)
N(4)−Fe1−N(24)	84.6(2)	85.11(13)	83.55(13)
N(21)−Fe1−N(22)	75.0(3)	75.49(15)	79.32(14)
N(21)−Fe1−N(24)	155.8(2)	156.79(14)	167.79(14)
N(22)−Fe1−N(24)	83.4(3)	83.86(14)	90.15(15)

Results

Structural Properties. The structure of the title compound was solved in both high-spin [$S = 2$ (270 and 240 K)] and low-spin states [$S = 0$ (120 K)]. The cooling rate was 2 K/min. Upon lowering the temperature, the structural parameters changed, but no modification of the structure type was observed. The space group $P2_1/n$ remained unchanged for both high-spin and low-spin states, however, with noticeable structural changes, mainly for the β angle (Table 1). Selected bond lengths and angles are summarized in Table 2. Notably, the color of the crystal changed from yellow (HS) to reddish brown (LS).

The structure reveals meridional tridentate coordination of the ligand similar to cobalt(II) and nickel(II) complexes.[3] The asymmetric unit contains a cationic moiety (ligand-bound Fe^{II}), two perchlorate anions, and a toluene molecule as the solvent of crystallization. A perspective view of the molecule in the HS state (270 K) is displayed in Figure 1. As stated earlier, the structure of the compound was obtained at two different temperatures, 270 and 240 K, in the high-spin phase. Surprising differences were revealed in the degree of disorder of the solvent of crystallization and perchlorate ions. At 270 K, all carbon atoms of the toluene molecule are disordered over two equivalent positions (50% occupancy factors). However, at 240 K, only two carbon atoms of the toluene molecule and all oxygen atoms of the perchlorate anions are disordered (50% occupancy factors). On the other hand, no sizable difference in metric parameters is observed between 270 and 240 K. At 270 K, the average $Fe-N_{pyridine}$ bond lengths 2.183(5)/2.225(5) Å (Fe−N1/N4/N21/N24) are longer than average $Fe-N_{pyrazole}$ ones, 2.038(5) Å (Fe−N2/

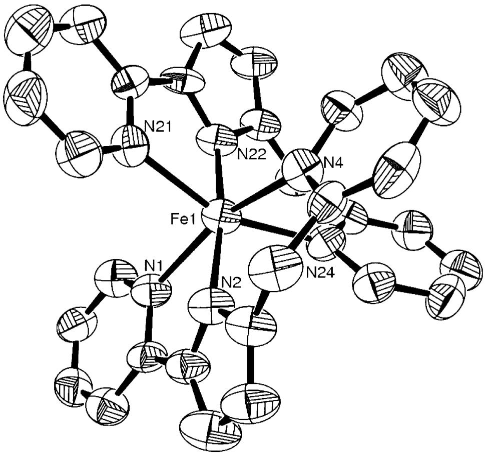

Figure 1. Perspective view of the crystallographically independent dication in the crystal of [Fe(L)$_2$][ClO$_4$]$_2$·C$_7$H$_8$ at 270 K showing the atom numbering. Atoms are drawn at the 40% probability level. Hydrogen atoms are omitted for clarity.

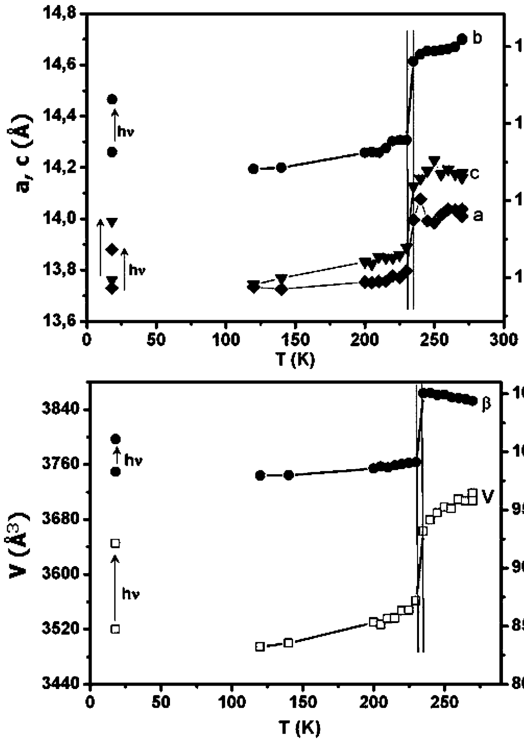

Figure 2. Temperature dependence of the lattice parameters *a*, *b*, and *c* (top) and the unit cell volume *V* and angle *β* (bottom) for [Fe(L)$_2$][ClO$_4$]$_2$·C$_7$H$_8$. Lines are a guide for the eyes, and the spin-transition temperature range is indicated by vertical bars. Arrows at 18 K indicate the structural changes induced by 532 nm laser irradiation associated with the LIESST effect.

N22), and they are typical of high-spin Fe^{II} complexes. The iron(II) environment has a distorted octahedral geometry, as expected due to the nonplanar tridentate ligand, where the trans angle varies between 155.8(2) and 171.2(2)° while the cis angle spans over a wide range from 74.6(2) to 103.3(2)°. The overall distortion from an ideal octahedron can be expressed through the *octahedral distortion parameter*[24] Σ, equal to 84.6 (2)° here, which is on the higher side of the values reported for similar complexes.[6a,24c] On the contrary, the 120 K value $\Sigma = 58.1(1)°$ is in line with literature data for LS complexes, which generally have more regular geometry than their high-spin counterparts. Metric parameters at 120 K (Table 2) reflect usual shortening of the Fe–N$_6$ bond lengths upon the HS-to-LS transition. Fe–N$_{\text{pyridine}}$ bond lengths 1.986(3)/2.033(3) Å (Fe–N1/N4/N21/N24) shorten appreciably by 0.19 Å, while Fe–N$_{\text{pyrazole}}$ 1.877(3) Å (Fe–N2/N22) shortens by only 0.06 Å. This is associated with the donor character of the Fe–N$_{\text{pyridine}}$ bond, which is π-bonded to the metal ion to stabilize the LS state. In addition, the more regular geometry of the molecule in the LS state is reflected by the increase in cis and trans bond angles, where trans bond angles vary slightly from 167.78(12) to 172.26(13)° while cis angles span over a large range from 79.33(12) to 96.26(12)°.

We followed the transition by checking the temperature dependence of the unit-cell parameters. After cooling down to 120 K, the crystal was heated, and diffraction data were recorded every 5 K. The complete set of data is listed in Table S1 (Supporting Information). Temperature dependences of the lattice parameters (*a*, *b*, *c*, *V*, and *β*) are plotted in Figure 2. Dramatic changes can be observed in a narrow temperature range (230–235 K). Unusual features are the large and complex changes exhibited by the *β* angle. The discontinuous change of volume occurs between 230 and 235 K upon warming the sample and is a direct signature of the first-order nature of the phase transition. The discontinuous variation of intensity of a few Bragg peaks as a function of the temperature is given in Figure S1 (Supporting Information). The LIESST effect was investigated by X-ray diffraction at 18 K after laser excitation at 532 nm. During the LIESST effect, important variations of the lattice parameters were observed, consistent with that observed during the thermal spin-transition. The phototransformation of the crystal was found to be complete, as already observed on crystals of similar thickness,[25,32d] since partial conversion would give rise to the coexistence of LS and HS Bragg peaks, which was not observed. The values of lattice parameters in the photoinduced state (Figure 3) compare to those of the HS state at high temperatures. However, the photoinduced changes appeared to be sizeably smaller than those observed at the thermal transition. Unfortunately, the quality of the crystal suffered from the effects of phototransformation and did not allow for performing the desired complete structural analysis.

Magnetic Measurements. The magnetic behavior of [Fe^{II}(L)$_2$][ClO$_4$]$_2$·C$_7$H$_8$ is shown in Figure 3 in the form of a $\chi_M T$ versus T curve, χ_M being the molar magnetic susceptibility and T the temperature. At room temperature, $\chi_M T$ is equal to 3.41 cm^3 K mol^{-1}, which is in the range of

---

(24) (a) Guionneau, P.; Brigouleix, C.; Barrans, Y.; Goeta, A. E.; Létard, J.-F.; Howards, J. A. K.; Gaultier, J.; Chasseau, D. *C. R. Acad. Sci., Ser. IIc: Chim.* **2001**, *4*, 161. (b) Guionneau, P.; Marchivie, M.; Bravic, G.; Létard, J.-F. *Top. Curr. Chem.* **2004**, *234*, 97. (c) Moubaraki, B.; Leita, B. A.; Halder, G. J.; Batten, S. R.; Jensen, P.; Smith, J. P.; Cashion, J. D.; Kepert, C. K.; Létard, J.-F.; Murray, K. S. *Dalton Trans.* **2007**, 4413.

(25) (a) Ichiyanagi, K.; Herbert, J.; Toupet, L.; Cailleau, H.; Guionneau, P.; Letard, J.-F.; Collet, E. *Phys. Rev. B: Condens. Matter Mater. Phys.* **2006**, *73*, 060408(R). (b) Trzop, E.; Buron-Le Cointe, M.; Cailleau, H.; Toupet, L.; Molnar, G.; Bousseksou, A.; Gaspar, A. B.; Real, J. A.; Collet, E. *J. Appl. Crystallogr.* **2007**, *40*, 158.

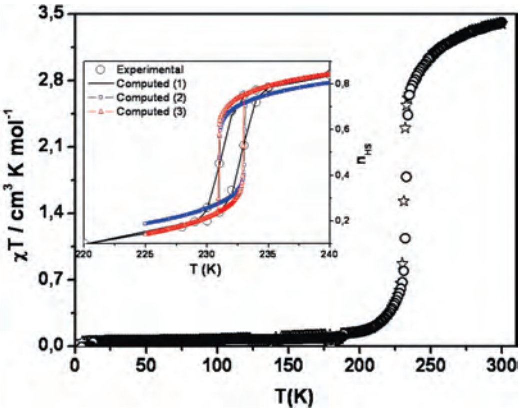

Figure 3. The spin equilibrium of $[Fe(L)_2][ClO_4]_2 \cdot C_7H_8$ from SQUID magnetization data under 1 kOe in the cooling and warming modes. The computed line with label (1) was obtained using the macroscopic variant of the two-level model. Computed lines (2) and (3), obtained using the microscopic variant of the model, illustrate the antagonistic effects of distribution width and interaction parameter, see discussion.

values expected for HS Fe^{II} ions, and below 200 K it is in the range of LS Fe^{II} ions. The transition is first-order, with a 2 K wide thermal hysteresis: $T_{1/2}$ (↓) ~ 231 K, $T_{1/2}$ (↑) ~ 233 K, with the latter in good agreement with X-ray data. The steep and sharp hysteresis confirms the presence of cooperative interactions in a well-crystallized system. However, sizable but continuous variations occur starting at 120 K and up to 250 K, a rather unusual feature in the spin-transition literature. All experimental features have been properly reproduced, see the inset of Figure 3, by using the macroscopic variant of the present model with a Gaussian distribution of electronic gaps. We used $\ln(g) = 7.65$ provided by the calorimetric investigation; we derived the mean electronic gap $\Delta_{el} = 1775$ K, from the measured transition temperature [$\Delta_{el} = T_c \ln(g)$], and we fitted the elastic interaction parameter $zJ = 249$ K and the Gaussian width of the distribution $\sigma(\Delta_{el}) = 5$ K. Alternative fits were considered on the basis of the microscopic variants of the model. A major feature is that the microscopic variants can keep the square character of the hysteresis loop, provided that the smoothening effect of the microscopic distributions is compensated by an adequate increase in the interaction parameter. This effect was obtained, see the "computed (2)" curve in Figure 3, without a substantial loss of the overlap to the experimental conversion curve on both sides of the loop. For example, the 2 K wide hysteresis loop of the thermal transition was obtained with the distribution width value inspired by the coming photomagnetic data, $\sigma(\Delta_{el}) = 260$ K, thanks to a sizable increase in the interaction parameter value, up to $zJ \sim 310$ K. In a second step, the combination of the present microscopic distribution with the previous macroscopic distribution would give the computed loop the desired bent shape, and finally it would lead to a good overlap of the experimental data. For the needs of further discussion, we also tried a broader distribution with $\sigma(\Delta_{el}) = 640$ K, see the "computed (**3**)" curve in Figure 3, which led to a drastic increase in the interaction parameter value, up to $zJ \sim 498$ K, and which induced visible discrepancies with the experimental conversion curve on both sides of the hysteresis loop.

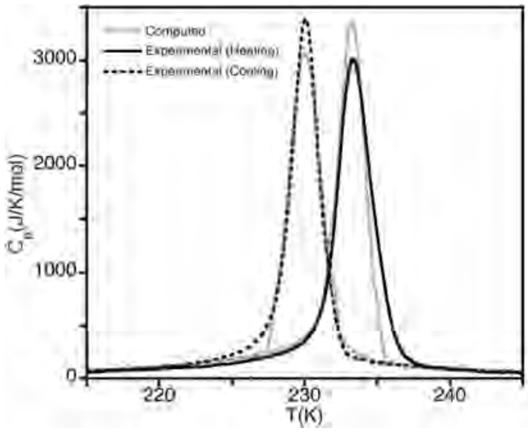

Figure 4. Temperature dependence of the heat capacity for $[Fe(L)_2][ClO_4]_2 \cdot C_7H_8$ obtained through differential scanning calorimetry: experimental data (thick lines) and computed curves using the macroscopic variant of the two-level model (thin lines). Heating and cooling branches are represented by full and discontinuous lines, respectively.

Mössbauer Measurements. The temperature dependence of the ^{57}Fe Mössbauer spectra has been studied between room temperature and 77 K. A selection of representative spectra is presented in Figure S2 (Supporting Information), and the fitted Mössbauer parameters are in Table S2 (Supporting Information). The absorption spectrum at 295 K consists of only one doublet with δ (*isomer shift*) = 0.95(1) mm s^{-1} and Δ (*quadrupole splitting*) = 1.46(1) mm s^{-1}, assigned to HS Fe^{II}; for that at 77 K, $\delta = 0.46(1)$ mm s^{-1} and $\Delta = 1.28(1)$ mm s^{-1}, assigned to LS Fe^{II}. At intermediate temperatures, we observed the coexistence of LS and HS contributions. The HS fractions n_{HS} derived from the relative absorption areas agree with the magnetic data.

DSC Calorimetry. The DSC response in both warming and cooling modes is displayed in Figure 4. The measurements shown here were done at 1 K/min for both cooling and heating rates and basically confirm the magnetic investigation (see above). The slightly larger thermal hysteresis of 3 K presumably results from a larger thermal inertia of the device. The enthalpy and entropy molar variations were found: $\Delta H = 12.95-13.56$ kJ/mol and $\Delta S = 55.8-58.77$ J/mol K in the heating and cooling modes, respectively. A correction was introduced for the incomplete character of the spin transition over the integration temperature range [$\Delta n_{HS} \sim 0.89$ for (202−261 K) upon heating, $\Delta n_{HS} \sim 0.91$ for (197−282 K) upon cooling], in order to refer to the complete conversion of 1 mol, as needed for the model: $\Delta H_{corr} = 14.55-14.90$ kJ/mol and $\Delta S_{corr} = 62.7-64.58$ J/mol K in the heating and cooling modes, respectively. After averaging the heating and cooling data, we derived the parameter values $\ln(g) = \Delta S_{corr}/R = 7.65$ and $\Delta_{el} = \Delta H_{corr}/N = 1771$ K. The observed entropy variation, 63.6 J/mol K, is obviously larger than the theoretical electronic contribution, $R \ln 5 = 13.4$ J/mol K, and clearly reflects the dominating role of vibrational contributions, as usually found for spin-transition systems.[26] The experimental data have been

---

[26] (a) Sorai, M.; Seki, S. J. *Phys. Chem. Solids* **1974**, *35*, 555. (b) Bousseksou, A.; McGarvey, J. G.; Varret, F.; Tuchagues, J.-P.; Dennis, A.-C.; Boillot, M.-L. *Chem. Phys. Lett.* **2000**, *318*, 409. (c) Sorai, M. *Pure Appl. Chem.* **2005**, *77*, 1331.

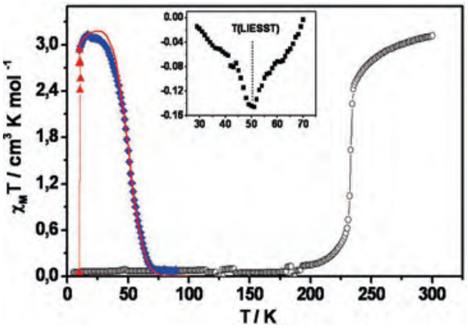

Figure 5. *T*(LIESST) experiment recorded for solvated compound [Fe(L)$_2$][ClO$_4$]$_2$·C$_7$H$_8$. The temperature dependence of $\chi_M T$ recorded in the cooling mode without irradiation is symbolized by open circles; the change recorded during 1 h of irradiation at 10 K corresponds to the triangle data points, and the behavior recorded during the warming mode (0.3 K min^{-1}) in the dark is shown by square data points. The full line curve was computed using the two-level model with $zJ = 0$, see text.

properly reproduced with the macroscopic model previously used for the magnetic hysteresis. The fitted parameters $zJ = 251$ K and $\sigma(\Delta_{el}) = 7$ K are slightly on the higher side. The larger *J* reflects the broader hysteresis, while the larger width of distribution might be assigned to instrumental effects such as a slight temperature gradient or inhomogeneous stresses induced by processing of the pellet. Further fits inspired by the coming photomagnetic data, using the microscopic variant of the model, are also shown in Figure 3.

Photomagnetism. The LS → HS photoconversion for both solvated and nonsolvated samples has been investigated using a SQUID magnetometer, coupled to an optical source, and also by diffuse reflectance spectroscopy. For both samples, a drastic increase of the magnetic signal under light irradiation (514.5 nm) at 10 K was observed. The photostationary value reached after typically 1−2 h was close to 3.0 cm^3 K mol^{-1} for the solvated sample and 3.2 cm^3 K mol^{-1} for the nonsolvated one. Figure 5 presents the *T*(LIESST) curve for the solvated sample, which was obtained by switching off the light when the signal was saturated and heating up the sample at a scan rate of 0.3 K min^{-1}. Similar data for the nonsolvated sample is presented in Figure S3 (Supporting Information). The initial increase of $\chi_M T$ in the range 10−25 K is attributed to the zero-field splitting effect of HS Fe^{II}. Both compounds reach a plateau in the temperature range 25−35 K, *ca.* 3.25 cm^3 K mol^{-1} for the solvated sample and 3.4 cm^3 K mol^{-1} for the nonsolvated sample, showing that phototransformation was almost complete. Further warming induced the thermal return to the stable LS state, which characterizes the onset of thermally activated relaxation. The minimum value of d$\chi_M T$/d*T* versus *T* plots, which characterizes the *T* (LIESST) temperature,[21] was obtained at ∼50 K for both compounds. The shapes of the *T*(LIESST) curves are broad, particularly in the case of the nonsolvated sample. Such a broad character is discussed and modeled, considering the isothermal relaxation curves in the following section. We briefly comment on the value *T*(LIESST) = 50 K, in the light of literature data [*T*(LIESST) versus $T_{1/2}$ plot; Figure 3 of ref 21b]. The data for the present compound lie on the $T_0 = 120$ K line, that is, 30 K lower than that expected for compounds with rigid tridentate ligands[27] ($T_0 = 150$ K line). Similar results were also found for [Fe(L′)$_2$][ClO$_4$]$_2$·H$_2$O[9] [L′ = 2,6-bis(pyrazol-1-yl-methyl)pyridine] and [Fe(L″)$_2$][BF$_4$]$_2$·MeOH[6a] [L″ = 2-(1-pyridin-2-ylmethyl-1H-pyrazol-3-yl)-pyrazine]. In all of these compounds, the ligands are conformationally flexible due to the presence of methylene spacers between the aromatic rings of the ligands (i.e., pyrazole and pyrazine). This emphasizes the concept that vibrational aspects and rigidity of the inner coordination sphere (through in-built flexibility of the ligands) are the key factors needed to govern the lifetime of the light-induced metastable HS state.

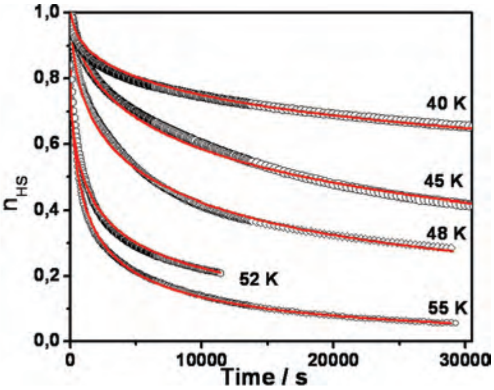

Figure 6. Isothermal relaxation curves of the solvated compound. Solid lines represent computed curves using the two-level model with $zJ = 0$, see text.

Relaxation Kinetics. The relaxation kinetics of the HS → LS conversion occurring after the LIESST effect were investigated for both solvated and nonsolvated compounds in the range 10−55 K. The decay of the normalized HS molar fraction, n_{HS}, versus time at various temperatures is presented in Figure 6 for the solvated compound. The most striking feature of these relaxation curves is their stretched exponential shape (fast initial decay followed by slower decay) instead of the sigmoidal shape expected for a cooperative system. Such stretched exponential shapes are typical for a broad distribution of relaxation times, which are expected to be associated with structural disorders (see above). The relaxation curves for the solvated compound have been satisfactorily fitted (solid lines in Figure 6) by a simplified variant of the master equation, dropping the LS → HS relaxation and the self-acceleration effect but accounting for a Gaussian distribution of activation energies (in the absence of interactions, the distinction between microscopic and macroscopic distributions is pointless). We determined the set of parameter values in several steps. In the first step, we treated independently the various relaxation curves, and for each of them, we fitted the width of barrier energy distribution and the time scale factor, which behave as weakly correlated parameters due to their obviously different impacts on the relaxation curve. Values of the distribution width, $\sigma(E_{HL})$, in the range 115−150 K provide both a rather good overlap of the experimental data (Figure 6) and a convenient

---

[27] (a) Money, V. A.; Costa, J. S.; Marcen, S.; Chastanet, G.; Elhaïk, J.; Halcrow, M. A.; Howard, J. A. K.; Létard, J.-F. *Chem. Phys. Lett.* **2004**, *391*, 273. (b) Elhaïk, J.; Kilner, M. A.; Halcrow, M. A. *Dalton Trans.* **2006**, 823.

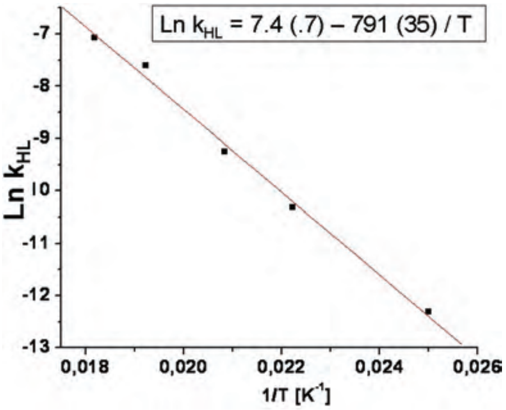

Figure 7. Arrhenius plot of $\ln(k_{HL})$ versus $1/T$: experimental data (■), linear regression (—) for $[Fe(L)_2][ClO_4]_2 \cdot C_7H_8$.

Arrhenius plot of the time scale factor (Figure 7), leading to the apparent activation energy $E_{HL} \sim 790$ (30) K and pre-exponential factor $\ln k_\infty \sim 7.4$ (0.7) [i.e., k_∞ in the range 750−3300 s^{-1}]. The experimental *T*(LIESST) curve could be conveniently simulated, see the solid line in Figure 5, by using average value $\sigma(E_{HL}) = 130$ K, pre-exponential factor $k_\infty = 1600$ s^{-1}, slightly reduced value $E_{HL} = 740$ K, *Lande g* factor = 2.08, and zero-field-splitting parameter $D = 7$ K.

As a matter of fact, for most of the relaxation curves, we were confronted with detectable discrepancies at short times, which in principle might be resolved by expanding the low-energy side of the distribution. However, the presence of low-energy barriers raised numerical problems since it drastically increased the computation time and finally dissuaded us from using asymmetrical distributions. Relaxation curves for nonsolvated compounds were also found in the shape of stretched exponentials (Figure S4, Supporting Information) with even broader energy distributions, which increased the mentioned numerical difficulties and prevented us from meaningful fitting

We also tried alternative fits of the relaxation curves accounting for the presence of interactions, in the frame of the microscopic variant of the cooperative model, with the final aim of modeling both the thermal hysteresis and the photomagnetic properties with the same set of physical parameters. By numerical simulations (Figure 8), we confirmed the opposite effects of interaction and distribution width parameters, already mentioned in the previous work.[10] For example, the introduction of $zJ = 250$ K (the thermal transition value) led to a dramatic increase of the barrier energy distribution width up to $\sigma(E_{HL}) \sim 320$ K, with a moderate reduction of the overlap with the experimental data (see Figure 8). As with the noncooperative case, we could also obtain rather good agreement with the experimental *T*(LIESST) curve (see inset to Figure 8) by using the corresponding set of parameters $zJ = 250$ K, $\sigma(E_{HL}) \sim 320$ K, and $k_\infty = 700$ s^{-1}, with again a slight reduction in the barrier energy value $E_{HL} = 715$ K. A close inspection of Figure 8 shows that the introduction of interactions has slightly reduced the overlap to experimental data. Clearly, the *T*(LIESST) curve as well as the set of relaxation curves do not provide sufficient information for really disentangling the antagonistic parameters *zJ* and $\sigma(E_{HL})$. More complete information is expected from the LITH data. However, their determination by photomagnetic measurements should face the difficult problem of the bulk absorption of light.[28] Determination by the reflectivity technique also raises questions (see below).

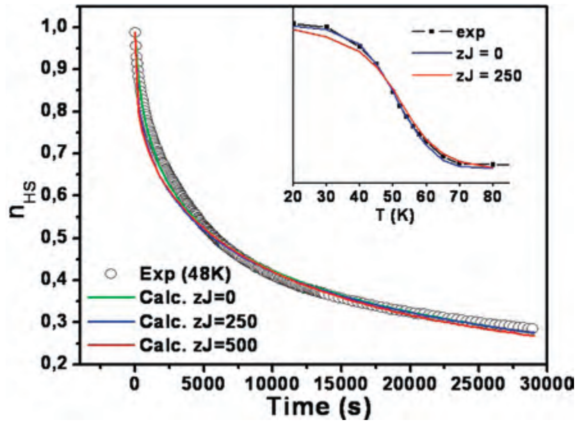

Figure 8. Alternative fits of the relaxation curve at 48 K, using the microscopic variant of the model, with various values of the interaction parameter ($zJ = 0$, 250, 500 K), again illustrating the antagonistic effects of distribution width and interaction parameter. Inset: the *T*(LIESST) curve computed with and without the interaction parameter, compared to the experimental data.

We finally reached the conclusion that the properties of the system could not be modeled using a temperature-independent set of parameters. Indeed, the minimum $\sigma(E_{HL})$ value (320 K) associated with the relaxation curves is inconsistent with the thermal hysteresis data. This is due to a consideration of the energy gap distribution $\sigma(\Delta_{el})$, which is expected to be twice as broad as $\sigma(E_{HL})$ according to theoretical models.[29] We showed in Figure 3, computed line (3), that a transition curve computed with $\sigma(\Delta_{el}) \sim 650$ K (and accordingly $zJ = 498$ K) overlaps less effectively with the experimental data. The discrepancies are obviously increased when, in turn, the relaxation curves are analyzed accounting for such a large value of the interaction parameter, which tends to dramatically increase the width of the barrier energy distribution, as previously shown in the present section. At last, the present difficulties were explained by the detailed structural data, reported in the last section, which provided direct evidence for the temperature-dependent character of both disorder and interactions in the system.

Diffuse Reflectance. For the solvated compound, we show in Figure 9 the thermal scan of the reflected intensity at 600 nm. As the scan rate was ~ 0.3 K min^{-1}, it was not expected to lead to drastic kinetic effects, at least above the previously determined *T*(LIESST) temperature of ~50 K. The data exhibit the typical features of a spin-transition compound, subjected to irradiation suitable for the LIESST effect. It revealed both the thermal spin-transition and low-temperature photoexcitation, together with large deviations with respect to the variation of the HS fraction (as determined by magnetic data). This in turn provided motivation for a complete

---

[28] Varret, F.; Nogùes, M.; Goujon, A. *Magnetism from Molecules to Materials*; Miller, J., Drillon, M.; Wiley-VCH: New York, 2001; Vol. 2, pp 257−295.

[29] Boukheddaden, K.; Shteto, I.; Hôo, B.; Varret, F. *Phys. Rev. B: Condens. Matter Mater. Phys.* **2000**, *62*, 14796.

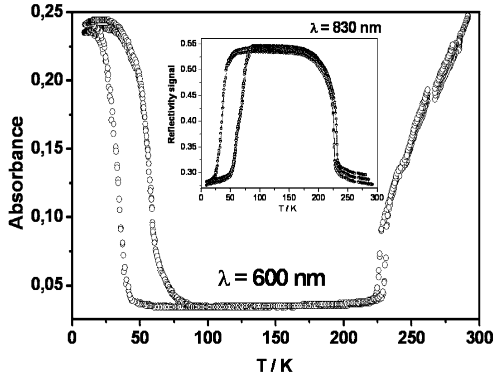

Figure 9. Thermal variation of reflectivity signal for [Fe(L)$_2$][ClO$_4$]$_2$·C$_7$H$_8$ recorded at 600 nm. Inset: thermal variation at 830 nm.

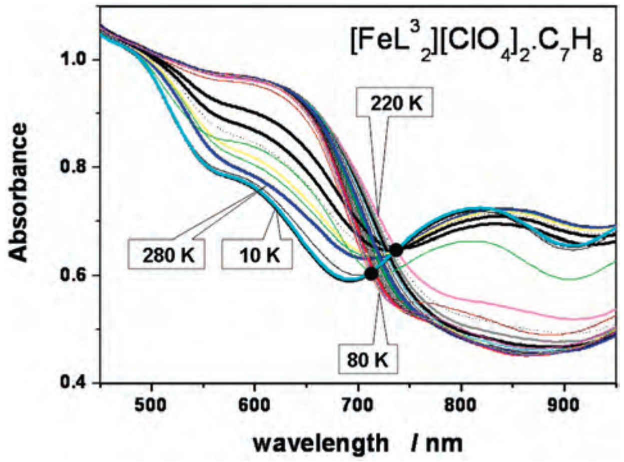

Figure 10. The complete set of diffuse reflectance spectra for [Fe(L)$_2$][ClO$_4$]$_2$·C$_7$H$_8$.

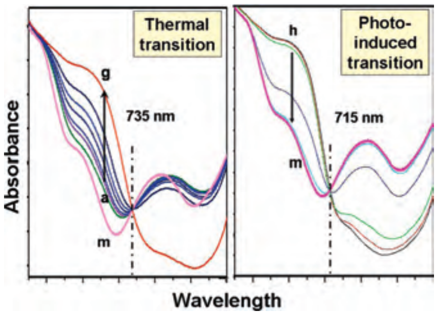

Figure 11. The diffuse reflectance spectra at the vicinity of the thermal transition (left-hand side, 280−220 K every 10 K) and of the photoinduced transformation (right-hand side, 80−10 K every 10 K), with their different isosbestic points. The curve of the low-temperature photoexcited state (m) fits both of them.

investigation of the absorbance spectra, which is presented below. The mentioned deviations obviously reflect unusual thermal evolution of the structure and might be correlated to the structural disorder. An experimental LITH loop can be observed at low temperatures, but all attempts to model this phenomenon with the sets of parameters used so far failed to reproduce the full width and square shape of the loop. This failure probably illustrates the impact of structural transformations suggested in the following section.

Reflectance spectra were recorded every 10 K, and the absorbance spectra were derived through the usual Kubelka−Munk treatment.[30] The complete set of spectra (Figure 10) was unusually complicated:

(i) A large blue-shift of the spectra is observed in the range 200−80 K, that is, in the saturated LS state, which we assigned to the stiffening effect associated with the thermal variation of disorder parameters.

(ii) Isosbestic points are observed in the vicinity of the thermal- and photoinduced transitions (Figure 11). The presence of an isosbestic point at the thermal transition seems to be the general rule for the thermal spin transition[31] and is usually explained by the coexistence of independent phases in variable amounts. This simple explanation might also hold for the photoinduced transition. The fact that isosbestic points are different at the thermo- and photoinduced phase transitions merely supports our previous conclusion about the failure in our attempts to model, with temperature-independent parameters.

(iii) We also noticed a strong similarity between the curves of the photoexcited and high-temperature HS phases (Figure 10), which suggests the presence of a high-temperature disorder in the photoinduced state—actually at a temperature higher than 280 K, if an intuitive extrapolation of the curves is accepted. This observation contributes to the present effort of crystallographers toward the comparison of thermo- and photoinduced HS structures.[32] It also leads to a consideration of the existence of a (frozen) large structural disorder, which is responsible for the broad distribution of relaxation rate constants. Accordingly, the relaxation process should account for structural effects, which are missing in the present relaxation model, which is purely electronic in nature. The recourse to more complex models combining spin-crossover and an order−disorder process[33] seems suitable, for future work.

Discussion

The various numerical simulations made so far have illustrated the antagonistic effects of cooperativity and disorder and complete the previous observations[8b] by con-

---

(30) (a) Kubelka, P.; Munk, F. *Z. Tech. Phys.* **1931**, *12*, 593. (b) Mirabella, F. M. *Modern Techniques in Applied Molecular Spectroscopy*; Wiley: New York, 1998. (c) Kortüm, G.; *Reflectance Spectroscopy*; Springer: New York, 1969.

(31) (a) Boillot, M.-L.; Chantraine, S.; Zarembowitch, J.; Lallemand, J.-Y.; Prunet, J. *New J. Chem.* **1999**, 179. (b) Sour, A.; Boillot, M.-L.; Rivière, E.; Lesot, P. *Eur. J. Inorg. Chem.* **1999**, 2117. (c) Hayami, S.; Sato, O.; Inoue, K.; Einaga, Y.; Maeda, Y. *J. Nucl. Radiochem. Sci.* **2002**, *3*, A1–A9; No. 2. (d) Loutete-Dangui, E. D.; Varret, F.; Codjovi, E.; Dahoo, P. R.; Tokoro, H.; Ohkoshi, S.; Eypert, C.; Létard, J.-F.; Coanga, J.-M.; Boukheddaden, K. *Phys. Rev. B: Condens. Matter Mater. Phys.* **2007**, *75*, 184425. (e) Boukheddaden, K.; Loutete, D.; Koubaa, M.; Eypert, C. *Phys. Status Solidi* **2008**, *5*, 1003.

(32) (a) Kusz, J.; Spiering, H.; Gütlich, P. *J. Appl. Crystallogr.* **2001**, *34*, 229. (b) Howard, J. A. K.; Goeta, A. E.; Chastanet, G.; Létard, J.-F.; Chasseau, D. *J. Am. Chem. Soc.* **2002**, *124*, 194. (c) Radosavljevic, E. I.; Halcrow, M. A.; Goeta, A. E.; Howard, J. A. K. *Chem. Commun.* **2003**, *1*, 158. (d) Huby, N.; Gúerin, L.; Collet, E.; Toupet, L.; Ameline, J.-C.; Cailleau, H.; Roisnel, T.; Tayagaki, T.; Tanaka, K. *Phys. Rev. B: Condens. Matter Mater. Phys.* **2004**, *69*, 020101 (R). (e) Okamura, H. *Phys. Rev. B: Condens. Matter Mater. Phys.* **2004**, *69*, 064104. (f) Legrand, V.; Pillet, S.; Carbonera, C.; Souhassou, M.; Létard, J.-F.; Guionneau, P.; Lecomte, C. *Eur. J. Inorg. Chem.* **2007**, 5693. (g) Oyanagi, H.; Tayagaki, T.; Tanaka, K. *J. Lumin.* **2006**, *119*, 361.

(33) Chernyshov, D.; Klinduhov, N.; Törnroos, K. W.; Hostettler, M.; Vangdal, B.; Bürgi, H.-B. *Phys. Rev. B: Condens. Matter Mater. Phys.* **2007**, *76*, 014406.

sidering distributions on the *microscopic* scale. The change from macroscopic to microscopic distribution in the mean-field cooperative system leads to a drastic reduction of the distribution effects and sets the comparison of the effects upon the thermal transition and the relaxation curves on a different basis. Here, the presence of distributions sizeably impacts both of these experimental features.

Let us just recall that disorder induces local perturbations of all physical parameters, among which the ligand field is usually considered as the most sensitive parameter. The ligand field finally modulates all physical parameters involved in the double-well description of the free energy of the spin-transition unit. In principle, the model should correlate the variations of barrier energies E_{HL}, E_{LH}, and of electronic gap Δ_{el}. In practice, these parameters have separate impacts on the physical properties: E_{HL} on low-temperature relaxation and Δ_{el} on the quasi-static thermal transition. Therefore, they could be introduced separately, but conversely little could be learned about their necessary correlations.

At variance with the macroscopic distributions, the microscopic distributions do not really smear out the sharp character of the thermal or LITH transitions, because the microscopic distribution effect is averaged at each computation step of the self-acceleration factor, due to the long-range character of the mean-field treatment. Distribution effects are compensated by an adequate increase of the interaction parameter.

The separate determination of the antagonistic factors appears to be a real challenge; in principle, these factors might be disentangled by a quantitative analysis of the LITH data, which display features separately attributable to the long-range elastic interactions (width of the loop) and to the spreading of physical parameters (slope of the lateral branches). As mentioned in the previous section, realistic models should account for both electronic and structural processes.

We now discuss the noncovalent interactions which are responsible for the large value of the interaction parameter $zJ = \alpha k_B T/2$ and the abruptness of the thermal transition in contrast to the nonsolvated compound. A closer inspection of the crystal packing diagrams of structures in the HS and LS state reveals that the molecule is engaged in a number of secondary interactions. Due to these interactions, the compound possesses various types of extended networks via $C-H\cdots\pi$ or $C-H\cdots O$, and the strength of the interactions is governed by the spin state of the compound and temperature dependence of the structure. Relevant bond distances, bond angles, and symmetry parameters are summarized in Table S3 (Supporting Information). The possible interactions with solvent molecules are depicted in Figure 12a, which reveals that there are two types of $C-H\cdots\pi$ hydrogen-bonding interactions: (i) one involving a meta C−H (H24) of the pyridine ring of the 3-(2-pyridyl)pyrazole unit in the ligand and π-electron cloud of the toluene molecule, labeled as type d1, and (ii) another involving two C−H's (H54 and H56) of the toluene ring interacting with the π-electron cloud of the pyridine ring of the 3-(2-pyridyl)pyrazole unit in the ligand, labeled as type d2. Similar investigations for possible intermolecular interaction assisted by perchlorate anions revealed that two oxygen atom(s) of the perchlorate anion interact very strongly with the hydrogen of the ligand molecules, as depicted in Figure 12b,c. Using these interactions, we determined the dimensionality of the interaction network, which happens to be temperature-dependent (Table 3). The interaction network is 3-D on both sides of the spin transition but becomes 2-D upon increasing the temperature due to the removal of the strong $C-H\cdots O$ interactions (labeled as d4), which propagated along *a* axis. We show in Figure S5 (Supporting Information) a perspective view of the network at 120 and 240 K. The thermal evolution of the interaction network adds to the complexity of the system under study. It may explain the little cooperative character of the relaxation curves, since the electronic interaction network is expected to be weak due to similarity to the HS phase at higher temperatures.

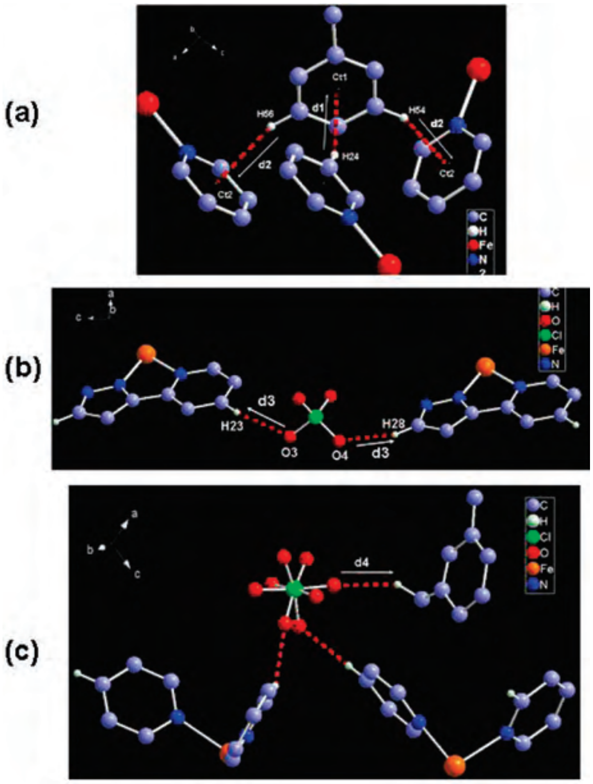

Figure 12. A perspective view of the possible (a) $C-H\cdots\pi$ and (b,c) $C-H\cdots O$ interactions in the dication $[Fe(L)_2]^{2+}$. All hydrogen atoms and other parts of the ligand except those involved in hydrogen bonding are excluded for clarity.

Conclusion

The present work adds a new example to those compounds where solvent molecules significantly change the spin-transition behavior. The spin-transition behavior of the present solvated compound has been investigated in great detail by various techniques, namely, photomagnetism, Mössbauer and diffuse reflectance spectroscopy, X-ray crystallography, and calorimetry. The spin-crossover behavior of the present system exhibited a surprising mixture of cooperative and disorder-like features: steep and hysteretic

Table 3. Summary of Noncovalent Hydrogen Bonding Interactions in $[Fe(L)_2][ClO_4]_2 \cdot C_7H_8$ at 270, 240, and 120 K, with the Propagation Axis of the Interaction, Allowing to Determine the Dimensionality of the Interaction Network[a]

	C−H···π interactions (threshold distance: 3.05 Å)				C−H···O interactions (threshold distance: 2.72 Å)				
T (K)	d1	d2′	d2″	axis	d3′	d3″	d4	axis	network
120	2.535(1)	2.624(1)	2.525(1)	*b*,*a*	2.275(1)	2.186(1)	*	*c*	3*D*
240	2.65(1)	2.830(1)	*	*b*	2.260(1)	2.144(1)	2.16(1)	*c*,*a*	3*D*
270	2.622(1)	2.725(1)	*	*b*	2.303(1)	2.286(1)	*	*c*	2*D*

[a] An asterisk (*) indicates that these distances could not be determined due to orientational changes in the lattice.

thermal transition due to elastic interactions and stretched exponential-shaped relaxation curves. The latter is typical for a distribution of relaxation rate constants and the presence of structural disorder, which has been identified. Interactions and disorder can be termed “antagonistic factors” since they have opposite effects on the cooperative behavior of the system. Indeed, we showed by numerical simulations using a microscopic variant of the usual mean-field model that the presence of disorder was compatible with the onset of sharp thermo- and photoinduced transitions, provided that the interaction parameter value was adequately increased. However, we could rule out the possibility of a temperature-independent set of parameters consistent with the present experimental data. We explained this challenging result by a detailed structure analysis at several temperatures, showing the occurrence of various degrees of disorder associated with the anion and solvent molecules’ positions. This led to the establishment of a strong temperature-dependence of the strength and dimensionality of the interaction network. A diffuse reflectance investigation supported such an unusual thermal evolution but also showed the similarity of the photo- and thermoinduced HS phases. Such a similarity led to the conclusion that structural aspects are deeply involved in the relaxation experiments through large disorder effects which offset the—presumably reduced—cooperative effect. We are inclined to believe that the unusual disorder effects may result from the synergistic effect between the conformational flexibility of the ligand and the presence of solvent molecules or counteranions in the lattice. Finally, we stress that in such a situation the refined values of the parameters should be considered to be highly model-dependent.

Acknowledgment. This work was supported by the European Union FP6-Network of Excellence MAGMANet and CEFIPRA (Contract IFC 3408-3; postdoctoral grant for V.M.). The authors would also like to thank the Région Aquitaine for development of an international platform of photomagnetism at the ICMCB (Bordeaux). Financial support is acknowledged from the Spanish MEC through the MAT2004-03395-C02-02 project. Acknowledgements are also due to Prof. K. Boukheddaden and Dr. I. Maurin for useful discussions about the comparison of photo- and thermoinduced high-spin phases.

Supporting Information Available: Complete set of crystallographic data (Table S1), fitted Mössbauer parameters (Table S2), noncovalent interaction parameters (Table S3), the discontinuous variation of intensity of a few Bragg peaks as a function of the temperature (Figure S1), representative Mössbauer spectra (Figure S2), *T*(LIESST) curve for a nonsolvated sample (Figure S3), relaxation curves for nonsolvated compound (Figure S4), and a perspective view of the network at 120 and 240 K (Figure S5). This material is available free of charge via the Internet at http://pubs.acs.org.

IC8002977